

Microstructure and Mechanical Properties of Laser-Welded Joints of Ti-22Al-25Nb/TA15 Dissimilar Titanium Alloys

Dalong Li, Shengsun Hu, Junqi Shen, Hao Zhang, and Xianzheng Bu

(Submitted June 28, 2015; in revised form January 27, 2016; published online March 28, 2016)

Laser beam welding (LBW) was applied to join 1-mm-thick dissimilar titanium alloys, Ti-22Al-25Nb (at.%) and TA15, and the microstructure and mechanical properties of the welded joints were systematically analyzed. Defect-free joints were obtained, and the fusion zone mainly consisted of B2 and martensitic α' phases because of the uneven distribution of the β phase stabilizer and rapid cooling rate of LBW. The phase compositions of the heat-affected zone varied with the different thermal cycles during the welding process. The different microstructures of the dissimilar titanium alloys led to an unsymmetrical hardness profile, with the welded seam exhibiting the lowest value of 271 HV. In room-temperature tensile tests, the fractures all occurred preferentially in the fusion zone. The strengths of the joints were close to those of the base metal but with prominently decreasing ductility. In tensile tests performed at 550 °C, all the joints fractured in the TA15 base metal, and the strength and plasticity of the welds were equivalent to those of the TA15 base metal.

Keywords dissimilar alloys, laser beam welding, mechanical properties, microstructure, titanium alloy

1. Introduction

In recent decades, extensive efforts have been devoted to developing titanium aluminide intermetallics. Among them, Ti₂AlNb-based alloys containing the ordered orthorhombic O phase, first discovered by Banerjee et al. in a Ti-25Al-12.5Nb (at.%) alloy (Ref 1), have attracted wide attention for their potential use in aircraft engines in addition to their outstanding properties such as high specific strength and fracture toughness and improved room-temperature ductility (Ref 2-7). Considering these excellent properties, second-generation Ti₂AlNb-based alloys were developed (Nb ≥ 25%, such as Ti-22Al-25Nb, Ti-22Al-27Nb). These alloys have been demonstrated to exhibit a higher service temperature capability compared with conventional titanium aluminide intermetallics (Ti₃Al (α_2)-based and TiAl (γ)-based alloys) and can provide a 40% weight reduction compared with nickel superalloys (Ref 8-10). To fully make use of the commercial potential of Ti₂AlNb-based alloys in aircraft (such as in the gas turbine systems), the establishment of appropriate welding procedures for both the self-joining of these alloys and their joining to conventional titanium alloys is of great significance (Ref 11-13).

It is restricted for dissimilar titanium alloys to choose an effective welding process, because of the lack of suitable filler metals. Only a few welding processes can meet the conditions, such as friction stir welding (FSW), laser beam welding (LBW), and electron beam welding (EBW). The weldability of Ti alloys by FSW is still at the stage of research (Ref 14). The preferred welding methods mainly focus on LBW (Ref 8, 15, 16) and EBW (Ref 17-19). Currently, some work exists on self-joining welding techniques for Ti₂AlNb-based alloys and joining techniques for Ti₂AlNb-based/titanium dissimilar alloys, such as Ti-22Al-27Nb, Ti-22Al-27Nb/TC4, Ti-22Al-25Nb/TC11, Ti3Al/TC4, and Ti-24Al-15Nb-1.5Mo/TC11 (Ref 11, 17-22). Tan et al. (Ref 17) investigated electron-beam-welded Ti-22Al-25Nb alloys and TC11, which contain three phases, B2 + O + α_2 , in the weld microstructure. These authors concluded that the room-temperature tensile strength of the joint is higher than that of the TC11 alloy. Lei et al. (Ref 11) applied LBW to a Ti-22Al-27Nb alloy and TC4. The weld metal consisted mainly of the B2 and martensitic α' phases. In addition, the average tensile strength of the joints was approximately 92% of that of TC4; however, the elongation of the joints was less than 40% of that of TC4.

Note that these investigations mainly focused on the welding of Ti₂AlNb-based alloys and $\alpha + \beta$ titanium alloys and only focused on the microstructure and mechanical properties at room temperature. In contrast, literature on the joining of a Ti₂AlNb-based alloy and a near- α titanium alloy is rare, especially systematic studies on the microstructure and properties at room and high temperature.

The TA15 alloy is a near- α titanium alloy that exhibits good weldability. Compared with TC4, this alloy exhibits a moderate strength at room and high temperatures and excellent high thermal stability with a slightly worse plasticity (Ref 23). This alloy is commonly used in manufacturing structural components of aircraft, such as gas turbine blades, nacelle center-beam frames, and large bulkheads. The ability to join the dissimilar metals of Ti-22Al-25Nb and TA15 alloys has

Dalong Li, Shengsun Hu, Junqi Shen, and Hao Zhang, Tianjin Key Laboratory of Advanced Joining Technology, Tianjin University, Tianjin 300072, People's Republic of China and School of Materials Science and Engineering, Tianjin University, Tianjin 300072, People's Republic of China; and Xianzheng Bu, Beijing Hangxing Technology Development Co., Ltd., Beijing 100013, People's Republic of China. Contact e-mail: shenjunqi@tju.edu.cn.

enormous potential in aerospace applications of Ti2AlNb intermetallic compounds.

Therefore, in this study, a LBW experiment was conducted on a 1-mm-thick Ti-22Al-25Nb/TA15 dissimilar alloy plate, and the microstructural characteristics, phase composition, element distribution, and mechanical properties of the laser-welded joints were systematically analyzed.

2. Experimental Procedure

The two dissimilar materials applied in the butt-welding experiment for the laser process were a Ti-22Al-25Nb alloy (Ti-11.1Al-42.2Nb, wt.%) and TA15 alloy (Ti-6Al-2Zr-1Mo-1V, wt.%), with the same dimensions of 200 mm × 100 mm × 1 mm. The melting point of the Ti-22Al-25Nb alloy is 1700 °C, and that of TA15 is 1670 °C. The microstructure of the Ti-22Al-25Nb alloy consisted of three phases, α_2 + B2 + O, with an equiaxed α_2 phase and lath O phase dispersed within the B2 matrix (bcc structure), shown in Fig. 1(a) and (b). The microstructure of TA15 is shown in Fig. 1(c); the black β phase is uniformly precipitated on the substrate of the white α phase.

The titanium alloy plate was fixed by a self-made clamp. Before welding, acetone and ethanol were used to clean the surfaces of the specimens. The butt-welding process was performed with a 4.0-kW YAG laser, and the LBW equipment was set in pulsed mode. The welding parameters were experientially selected for full-penetration butt welding (listed in Table 1). To prevent oxidation, argon of 99.99% purity was used as both the front and back shielding gas during welding with flow rates of 15 and 5 L/min, respectively.

The specimens for the metallographical analysis were wire cut perpendicular to the welding direction from the welded joints and then polished and etched using a Kroll solution (100 ml of H₂O, 3 ml of HF, and 5 ml of HNO₃). The subsequent microstructural observation and analysis were performed using an optical microscope (OM) and scanning electron microscope (SEM). The elemental distribution of the joint was determined using an energy dispersive spectrometer (EDS). The possible phases of the fusion zone and base metal were identified using x-ray diffraction (XRD). Hardness data were obtained using a microhardness tester with a load of 500 g and load time of 10 s. Tensile tests were performed at room temperature and an elevated temperature of 550 °C to evaluate the tensile strength of the dissimilar metal butt joints on a testing machine with a displacement speed of 2 mm/min. The loading direction was perpendicular to the welding direction, and the fusion zones were located at the center of the specimens. The geometries of the tensile specimens are

Table 1 Welding parameters employed in the welding process

Welding parameters	Values
Base power	700 W
Peak power	1300 W
Pulse duration	20 ms
Duty ratio	50%
Welding speed	1200 mm/min
Focal length of the lens	120 mm
Spot diameter	0.4 mm
Focal position	0 mm
Laser beam offset	0 mm

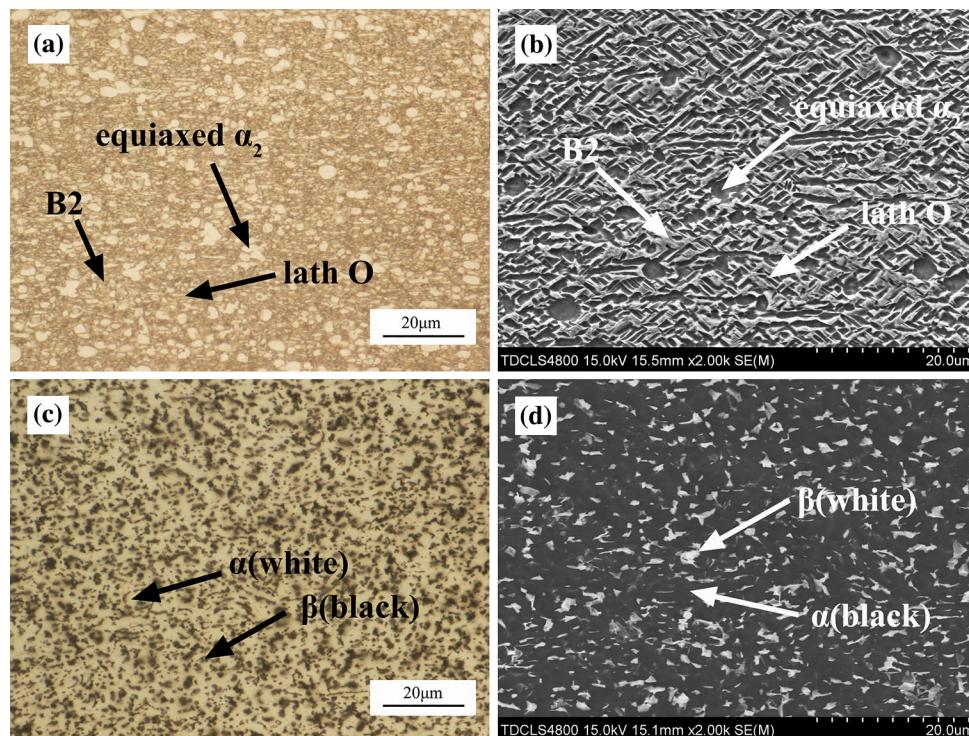


Fig. 1 Microstructures of the base metals: (a) OM and (b) SEM analysis of Ti-22Al-25Nb alloy and (c) OM and (d) SEM analysis of TA15 alloy

depicted in Fig. 2 (the units are mm). Finally, the fracture modes of the specimens were investigated by SEM.

3. Results and Discussion

3.1 Macromorphology of Welded Joints

Under the welding conditions of this study, defect-free full-penetration joints were obtained. The front and back appearances of the Ti-22Al-25Nb/TA15 dissimilar alloy welded joints were smooth (as observed in Fig. 3). No cracks or pores were observed on the surface of the weld metal. Both the front and back of the weld were a bright silver color with the protection of the shielding gas, which indicated that the surfaces of the weld were not contaminated with oxygen, nitrogen, or carbon. Figure 4 presents an OM macroscopic overview of the cross section of the weld. An asymmetric hourglass-shaped weld was

formed. The weld metal was extremely difficult to etch compared with the base metal and could thus be clearly distinguished from the base metal. Some dark semicircular-layered textures could be detected in the fusion zone and were approximately parallel to the fusion line. Similar dark layers have also been observed in other Ti3Al-based alloy joints formed using high energy density welding (Ref 20, 22, 24), which can be explained by the following phenomena. During crystallization in a molten pool, the latent heat of crystallization is constantly released and accumulated, resulting in a temporary pause of crystallization. The molten pool then cools down with rapid heat dissipation; with this temperature decrease, the crystallization restarts, resulting in a periodic process. During this process, the concentration of the low melting point solute in the metal liquid fluctuates periodically with the crystallization velocity, yielding segregation phenomena. The formation of the observed dark layers is due to this periodic element segregation (Ref 25, 26).

3.2 Microstructural Characterization of Welded Joints

3.2.1 Microstructure of Fusion Zone. The microstructure of the fusion zone was further examined, as shown in Fig. 5. No obvious second phase was observed, and the solidification structures were apparent. The microstructure mainly consisted of a large number of dendritic structures with the grains growing perpendicular to the direction of the radial fusion boundary (shown in Fig. 5a). As observed in Fig. 5(b), exiguous equiaxed grains are present in the center of the upside of the welded joints. The different microstructures of the two parts resulted from the diversity of the temperature gradient during the welding process. When solidifying starts, the direction perpendicular to the solid/liquid interface is the direction with the maximum temperature gradient and driving force for solidification, consequently generating a dendritic structure whose orientation is perpendicular to the solid/liquid interface. Before the end of solidification, the temperature gradient is very low at the center of the upside because of the release of the crystallization latent heat; therefore, exiguous and equiaxed grains could be obtained.

SEM, EDS, and XRD characterizations were used to identify the phases of the weld metal. Figure 6 shows the distribution of the different elements across the welded joint observed using an electron probe. The Ti content increases gradually from the left to the right along the fusion zone. The Nb content decreases rapidly in the fusion line near the Ti-22Al-25Nb alloy side and then fluctuates from approximately

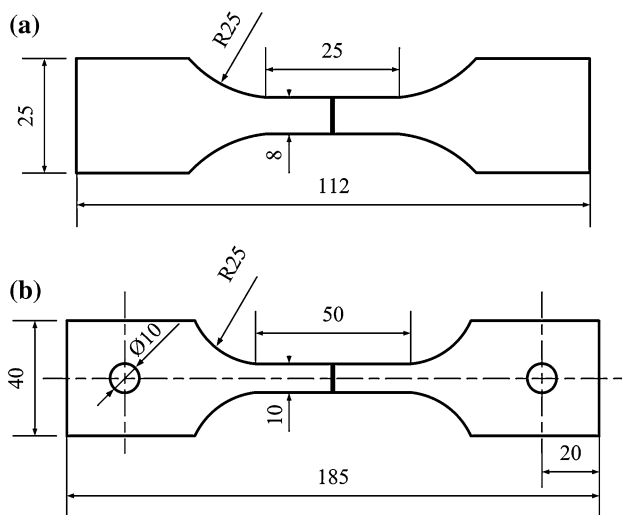


Fig. 2 Geometries of tensile test specimens for testing at (a) room temperature and (b) elevated temperature of 550 °C (the units are mm)

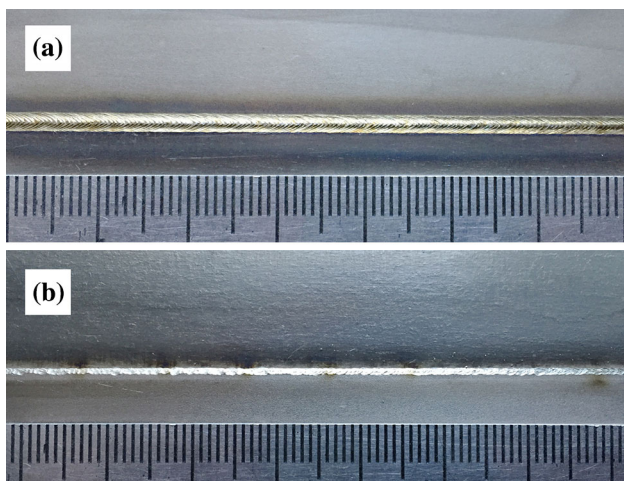


Fig. 3 Morphology of the welded joint: (a) front bead and (b) back bead

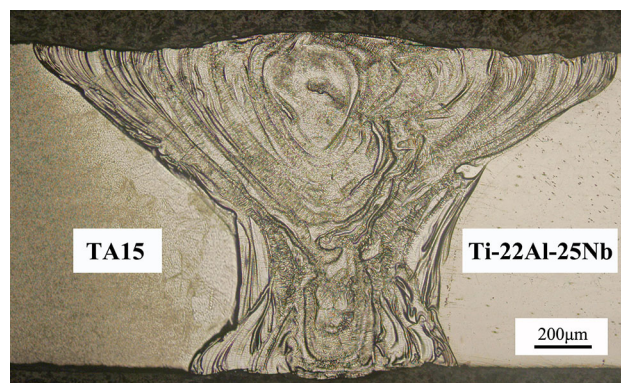


Fig. 4 Profile of the LBW butt joints

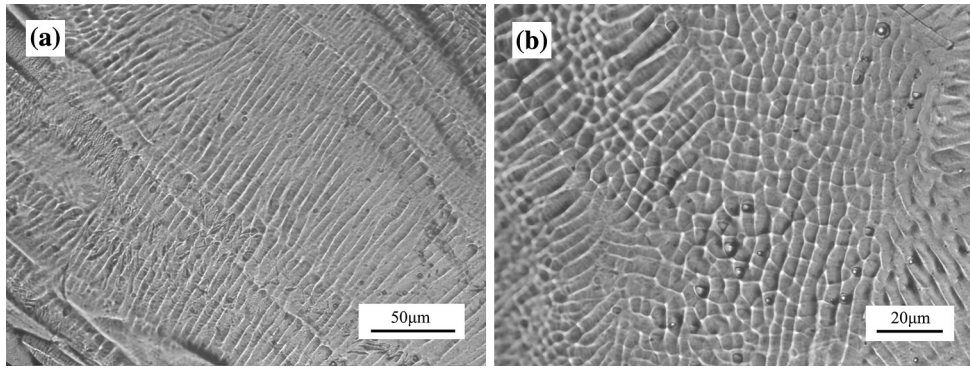


Fig. 5 Microstructure of the welded joint: (a) dendritic structure and (b) equiaxed grains

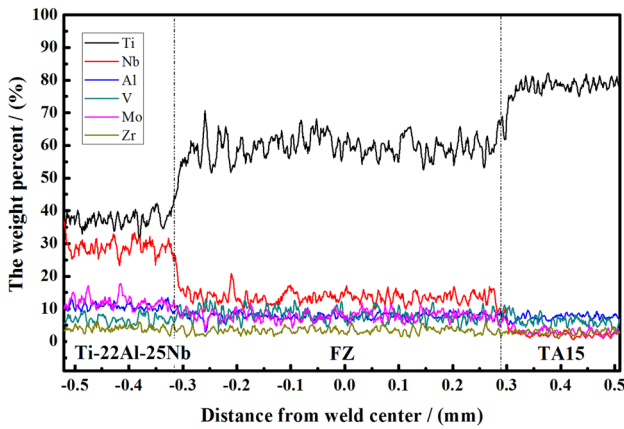


Fig. 6 Elemental distribution of the welded joint

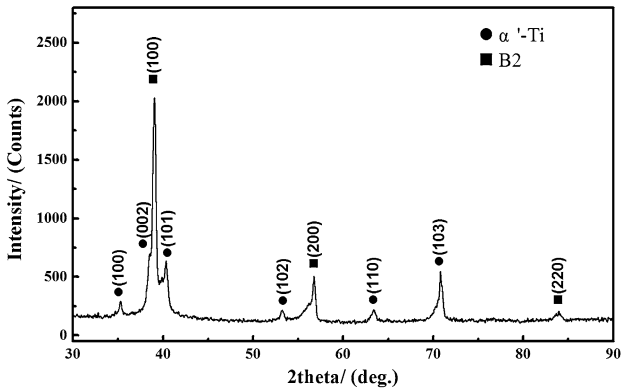


Fig. 7 XRD pattern of the welded joint

8.8 to 26.4% (wt.%) as the distance to the fusion line near TA15 alloy side decreases. The elemental distribution of Mo exhibits a similar trend as Nb. Compared with Ti and Nb, Al, V, and Zr are uniformly distributed. The differences in the elemental distribution were mainly caused by the components of the base metals. The EDS analysis revealed that the chemical composition of the fusion zone was Ti-15Al-7.6Nb-4Mo-2Zr-8V (at.%). According to Ref 27, elements such as Nb, Mo, and V may stabilize the β phase. The addition of 1 at.% Mo or V

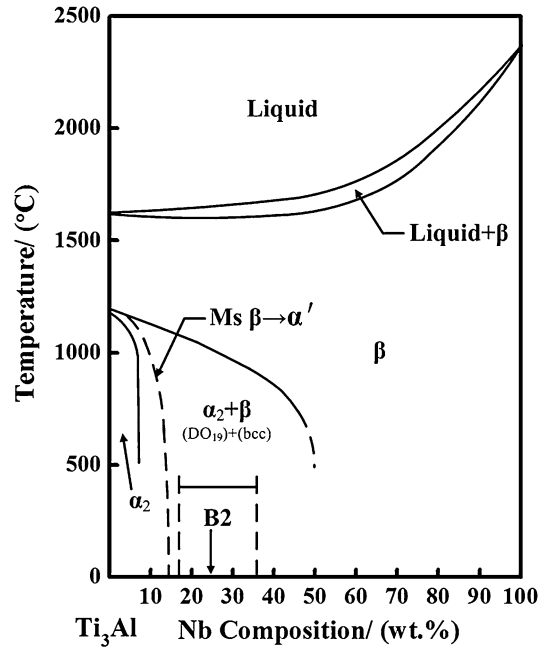


Fig. 8 Pseudo-binary diagram of the Ti₃Al + Nb system (Ref 28)

corresponds to the replacement of 4.25 or 1.58 at.% Nb, respectively, which indicates that more B2 phase can be stabilized at room temperature.

The XRD spectra (CuK α 1 radiation) of the weld metal is presented in Fig. 7, and diffraction peaks of the B2 phase and martensitic α' phase can be observed. According to work performed by Wu et al. (Ref 8), the weld microstructure consists primarily of the B2 phase when joining a Ti-24Al-17Nb alloy using the LBW process. The thermal cycle of EBW is similar to that of LBW in the welding process. Tan et al. (Ref 17) observed that the weld microstructure consisted primarily of the B2 phase and a large quantity of O/ α_2 particles during EBW of Ti-22Al-25Nb/TC11 dissimilar alloys. However, the laser-beam-welded joint of the Ti-22Al-25Nb/TA15 was mainly composed of the B2 phase and a small amount of martensitic α' . These results might be attributed to the different contents of the β phase stabilizer, especially the element Nb. The microconstituents and microstructural features of the weld metal can be better understood with the aid of the pseudo-

binary diagram of the Ti3Al-Nb system (Ref 28), presented in Fig. 8. In this experiment, the TA15 alloy diluted the β phase stabilizer in the weld; thus, the distribution of these elements was uneven. From the phase diagram, the M_s temperature is well below room temperature in alloys richer in Nb. Thus, the fusion zone containing more β phase stabilizer allows for the development of α_2 to B2 microstructures. Furthermore, for the high-Nb-containing Ti2AlNb-based alloy, the single B2 phase easily nucleated and grew when the β phase was rapidly cooled (Ref 29-32). Referring to the computed cooling rate at various LBW parameters, with the parameters employed in this paper, the cooling rate was much higher than the critical cooling rate of phase transformation, which inhibited the formation of other phases when β transformed into the B2 phase (Ref 24, 33). Thus, the weld metal and area near the heat-affected zone

(HAZ) mainly consisted of the B2 phase. Alloys containing less than 5 at.% Nb (11 wt.%) transform martensitically into the α' phase during rapid cooling from the β phase field, as demonstrated in Fig. 8. In this study, the β phase did not have enough time to transform into the α phase in the regions containing less β phase stabilizer as the temperature of the joint decreased rapidly and instead transformed into the supersaturated martensitic α' phase (Ref 34). Therefore, a small quantity of dispersed acicular martensitic α' phase can be observed in the fusion zone in the SEM image in Fig. 9.

3.2.2 Microstructure of Heat-Affected Zone. The microstructure of the HAZ was examined using OM and SEM. On the TA15 alloy side, an approximately 0.4 to 1.0-mm-thick region between the base metal and fusion zone can be easily identified as the HAZ (shown in Fig. 10a). Based on the different microstructures, the HAZ of the TA15 alloy can be divided into three regions, a recrystallization zone, fine-grain zone, and coarse-grain zone, locally magnified in Fig. 10(b) to (d). As the distance from the fusion zone decreases in the HAZ of the TA15 alloy, a clear reduction in the amount of β phase can be observed; in addition, the α phase gradually grows into a coarse microstructure, and a large amount of a dispersed acicular martensitic α' phase is formed in the HAZ near the fusion zone. The microstructural features of the HAZ in the TA15 alloy side can be better understood with the aid of Fig. 11.

In the recrystallization zone near the TA15 base metal zone, the peak heating temperature is higher than the recrystallization temperature (T_R , approximately 800 °C) but lower than the phase transformation temperature (T_P , approximately 980 °C). Recrystallization occurred with the coexistence of the new grains and primary grains (shown in Fig. 10b). In the recrystallization process, the solute dissolved into the grains but was unevenly distributed. Thus, more α phase precipitated from the β phase matrix.

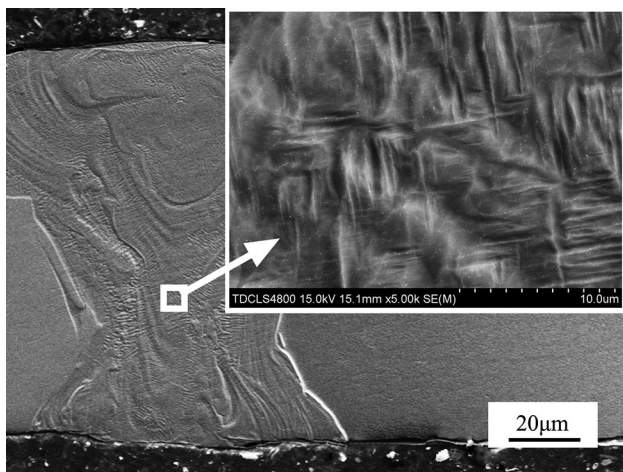


Fig. 9 SEM image of martensitic α' phase in the fusion zone

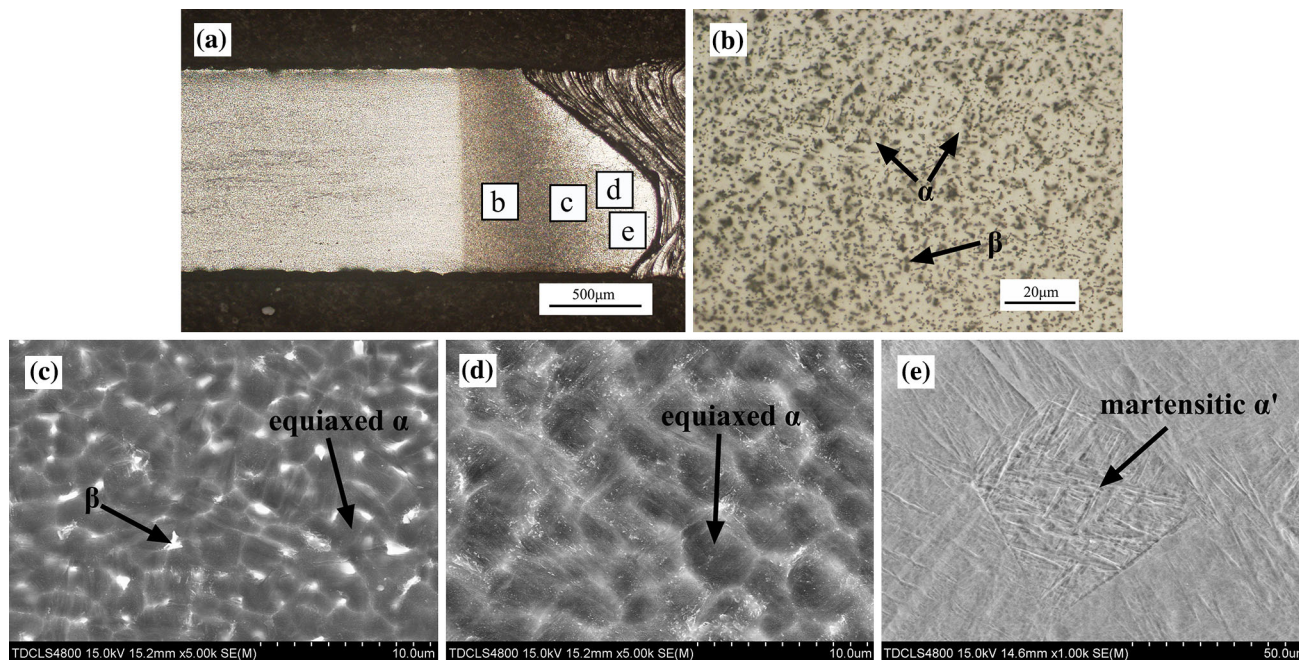


Fig. 10 HAZ microstructure of TA15 alloy: (a) overview, (b) recrystallization zone, (c) fine-grain zone, (d) coarse-grain zone, and (e) martensitic α' in coarse-grain zone

In the fine-grain zone, the peak heating temperature reached the temperature zone of the $\alpha + \beta$ phase or β phase but was lower than the grain coarsening temperature (T_G , approximately 1320 °C). Figure 10(c) demonstrates that the amount of α phase increased compared with that of the base metal, and the amount of the β phase significantly decreased. A fine and equiaxed α grain structure was obtained. During the heating process, the primary α phase transformed into the β phase. In the subsequent cooling process, the fine equiaxed α grains precipitated from the β phase matrix, and the β grain boundary gradually became fuzzy. Thus, the microstructure of the fine-grain zone consisted of equiaxed α phase and β phase.

In the coarse-grain zone near the fusion zone, the peak heating temperature exceeded the grain coarsening temperature. Massive grain coarsening and the disappearance of the β phase occurred in the grains with subsequent weld cooling, and this zone remained at a high temperature longer because of the low thermal conductivity of Ti alloys. Therefore, a large amount of coarse α phase was retained when the temperature dropped to room temperature. In the area closer to the weld, the transformed β phase could not transform into the equilibrium α phase through atomic diffusion because of the fast cooling rate and could only be transformed into the acicular martensitic α' phase via shear (shown in Fig. 10e) (Ref 35). Figure 10(d)

and (e) show the coarse α phase and martensitic α' in the coarse-grain region, respectively.

Figure 12 shows the microstructure of the HAZ in the Ti-22Al-25Nb alloy side. Strictly speaking, the HAZ in the Ti-22Al-25Nb alloy side should consist of three parts: a B2 single-phase zone, an $\alpha_2 + \text{B2}$ two-phase zone, and an $\alpha_2 + \text{O} + \text{B2}$ three-phase zone. However, no obvious boundaries were observed among the three parts (as illustrated in Fig. 12b) because of the narrow $\alpha_2 + \text{B2}$ two-phase zone and unstable O phase in the three-phase zone. Using the phase diagram of Ti-22Al-XNb (at.%) presented in Fig. 13 (Ref 36), the microstructure differences among each region in the HAZ can be better analyzed. In the HAZ near the fusion zone, the peak heating temperature was higher than the B2 transus temperature in the heating process; therefore, both the O phase and α_2 phase completely transformed into the B2 phase. However, the cooling rate was fast enough to suppress the disordered β phase into O/ α_2 phase transformations during the cooling process. Therefore, the region predominantly contained ordered B2 phase. As the distance to the fusion zone increased, the peak heating temperature decreased to the B2 + α_2 phase region from above the B2 transus temperature, and the B2 + α_2 phase could be retained at ambient temperature. Moreover, the $\alpha_2 + \text{B2}$ two-phase zone was too narrow to be identified in the

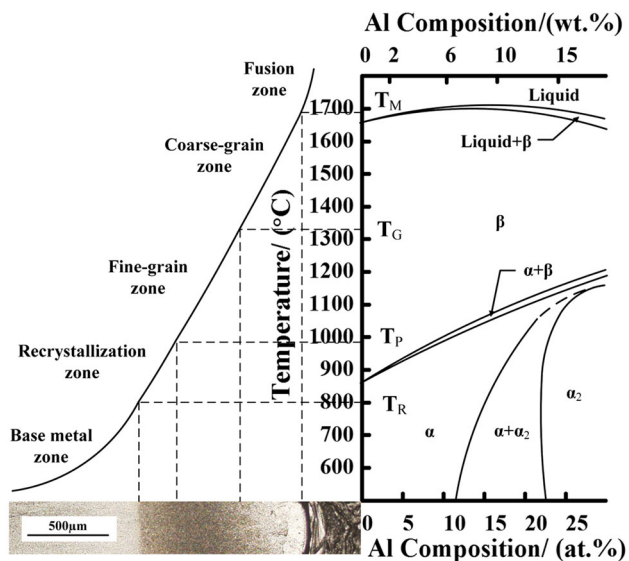


Fig. 11 Sketch of the HAZ on the TA15 alloy side

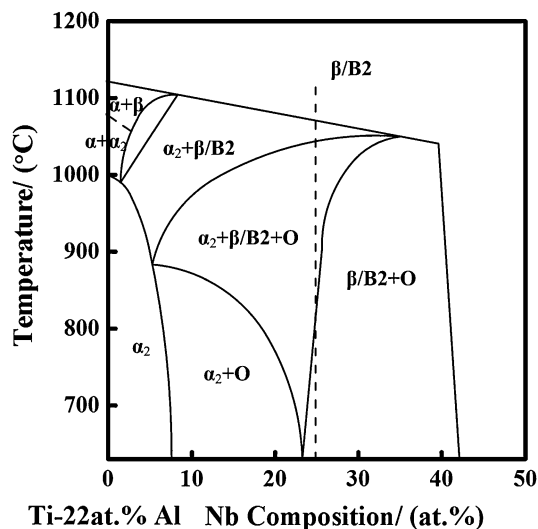


Fig. 13 Phase diagram of Ti-22Al-XNb alloys (Ref 36)

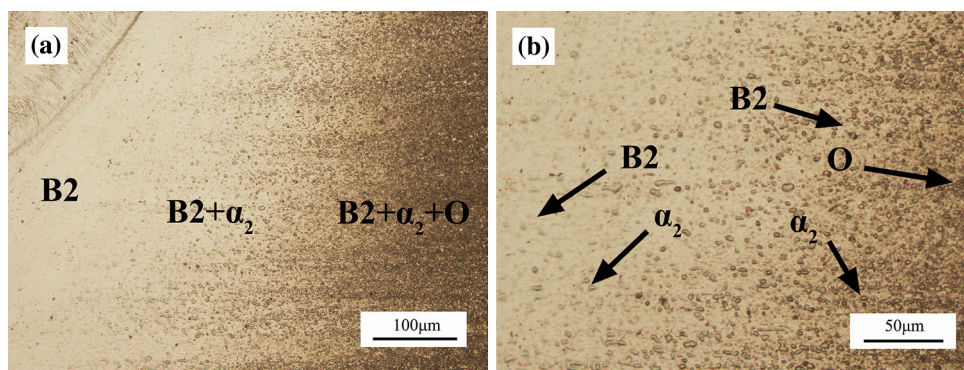


Fig. 12 HAZ microstructure of Ti-22Al-25Nb alloy: (a) overview and (b) high-magnification image

HAZ. In the HAZ adjacent to the base metal, the peak heating temperature dropped to the $\alpha_2 + O + B2$ three-phase range of the phase diagram. Because of the poor stability of O phase, the α_2 phase and a small amount of the O phase could be observed within the B2 matrix. Thus, the HAZ on the Ti-22Al-25Nb alloy side predominantly contains the B2 phase, and the α_2 phase and a small amount of the O phase are observed in the region adjacent to the base metal (shown in Fig. 12b).

3.3 Mechanical Properties of Welded Joints

3.3.1 Microhardness Measurement. The hardness distribution of the welded joint is shown in Fig. 14. Two hardness peaks appeared in the Ti-22Al-25Nb alloy and the HAZ of the TA15 alloy, which reached 384 and 376 HV, respectively. The welded seam exhibited the lowest hardness of 271 HV. On the Ti-22Al-25Nb alloy side, the hardness values of the HAZ were lower than those of the base metals. In contrast, the hardness of the HAZ of the TA15 alloy was higher than that of the TA15 base metal. The hardness distribution can be explained based on the microstructure of the welded joint. The welded seams were mainly composed of B2 phase and a small amount of martensitic α' . The hardness of the fusion zone is the lowest, because the soft phase B2 is far more than the hard phase α' .

On the Ti-22Al-25Nb alloy side, the HAZ and base metal predominantly contained the soft phase B2 and hard phase α_2/O . The O phase precipitated from the supersaturated solid solution of the B2 phase during solidification, with good compatibility between the phases. However, the differences in their spatial arrangement caused the coherent strain energy levels to rise, further resulting in obvious hardening. Thus, the values gradually increased when the hard α_2/O particle content in the soft B2 phase matrix increased with increasing distance from the fusion zone.

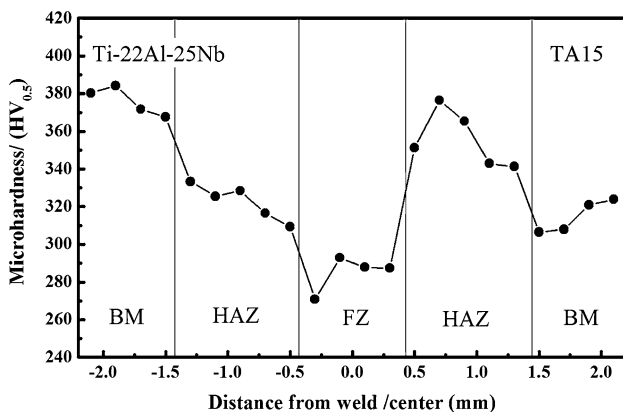


Fig. 14 Hardness distribution of the welded joint

According to the Hall-Petch relation, the hardness of metals increases with decreasing grain size. Compared with the grains inside the unaffected base metal, the grains in the recrystallization and fine-grain zones were finer. In addition, the finest grain size was observed in the fine-grain zone. Thus, the hardness of the base metal was lower than that of the other two regions, and the fine-grain zone exhibited the highest hardness on the TA15 alloy side. A second key factor is that the hardness of the existing phases in the TA15 alloys follows the order: martensitic $\alpha' > \alpha$ phase $> \beta$ phase (Ref 37). The coarse-grain zone mainly consisted of a mixture of martensitic α' and less primary α phase, which is the main reason for the hardness of the coarse-grain zone, which was higher than that of base metal despite the grain size being largest.

3.3.2 Tensile Properties. Tensile tests were conducted at room temperature and 550 °C for the welded joints and base metal. The tensile tests results, which are the mean value of three different specimens with the same welding parameters, are presented in Table 2. In the room-temperature test, the fractures all occurred preferentially in the fusion zone. The average tensile strength of the joints was 1019 MPa, which is 91.6% of that of the TA15 base metal. The average elongation was 2.05%, only reaching approximately 17.8% of that of the Ti2AlNb base metal. The ductility dramatically decreased. The corresponding fracture morphologies observed by SEM revealed mixed-pattern characteristics of river patterns and dimples (Fig. 16a). Brittle fracture traces and second-phase particles were observed on the tensile fracture surface following the massive dimples of various depths and



Fig. 15 Typical photograph of butt-welded joints after tensile testing at (a) room temperature and (b) 550 °C

Table 2 Tensile properties of base metal and welded joints

Test temperature	Tensile specimen	UTS, MPa	Elongation, %	Failure location
Room temperature	TA15 base metal	1112	11.58	...
	Ti-22Al-25Nb base metal	1179	11.50	...
	Welded joints	1019	2.05	Fusion zone
550 °C	TA15 base metal	695	15.1	...
	Ti-22Al-25Nb base metal	957	21.0	...
	Welded joints	714	14.3	TA15 base metal

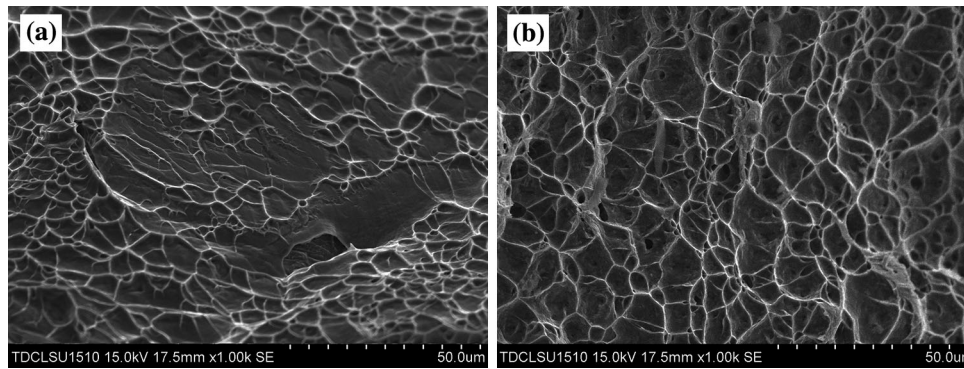


Fig. 16 SEM fractograph of the joint after tensile test at (a) room temperature and (b) 550 °C

sizes, implying that the fracture mechanism of the material was intergranular brittle fracture with dimple gliding fracture. In this study, the tensile behavior of the welded joints depended largely on the phase compositions and element segregation. The average tensile strength of the joints reached a relatively high level with the B2 and martensitic α' phases in the weld. According to work conducted by Lei et al. (Ref 11), the presence of the martensitic α' phase resulted in the increase of the average tensile strength and decrease of the ductility in the fusion zone. In addition, the nucleation of cracks preferentially initiated at the grain boundaries. Because the alloy elements were distributed unevenly in the B2 matrix, the element segregation at the grain boundaries further reduced the interfacial strengths (Ref 22).

In the tensile tests at 550 °C, all the joints fractured in the TA15 base metal. The fracture appearance is that of 45° shear fracture (shown in Fig. 15). The average tensile strength of the joints reached 714 MPa, with an average elongation of 14%, similar to those of the TA15 base metal but lower than those of the Ti-22Al-25Nb base metals. The tensile specimens of the joints were composite structures, consisting of zones of two different base metals, the HAZ, and the weld metal. The ultimate tensile strength of the welded joint was determined by the weakest part, with the other parts remaining in the elastic deformation stage during the entire tensile test. The fracture occurred in the TA15 alloy base metal at 550 °C, which indicates the higher-temperature tensile property of the orthorhombic B2 phase matrix in the weld metal and Ti-22Al-25Nb base metals compared with that of the TA15 base metal (Ref 38). Figure 16(b) shows the typical ductile dimple fracture pattern of the welded joints, with features of plastic fracture. The dimples are more numerous, smaller, and deeper than those in the fractograph at room temperature, which indicates the better plasticity of the tensile fracture at 550 °C.

4. Conclusions

Based on the experimental results and discussions, the following conclusions were drawn:

1. Defect-free full penetration of Ti-22Al-25Nb/TA15 dissimilar alloys welded joints was achieved using the LBW process.
2. The fusion zone mainly consisted of the B2 and martensitic α' phases because of the uneven distribution of the

β phase stabilizer and rapid cooling rate. The microstructure of the HAZ of the TA15 alloy consisted of primary α phase, β phase, equiaxed α phase, and acicular martensitic α' phase. The microstructure of the HAZ of the Ti-22Al-25Nb alloy consisted of the B2 and α_2 phases and a small amount of the O phase.

3. The hardness values in the HAZ of the Ti-22Al-25Nb alloy were lower than those of the base metals. In contrast, on the TA15 alloy side, the hardness values of the HAZ were higher than those of the base metals. The welded seams exhibited the lowest hardness values in the welded joint.
4. The fractures all occurred preferentially at the welded seams at room temperature. The average tensile strength of the joints was 92% of that of the TA15 base metal, and the average elongation only reached approximately 20% of that of the Ti-22Al-25Nb base metal, with dramatically decreasing ductility. Tensile tests at 550 °C revealed that the average tensile strength of the joint was equal to that of the TA15 base metal, the fracture occurred in the TA15 base metal, and the ductility was close to that of the TA15 base metal. The fracture pattern was a typical dimple fracture pattern, with features of plastic fracture.

Acknowledgments

The authors would like to gratefully acknowledge the support of Beijing Hangxing Technology Development Co., Ltd.

References

1. D. Banerjee, A.K. Gogia, T.K. Nandi, and V.A. Joshi, A New Ordered Orthorhombic Phase in a Ti3Al-Nb Alloy, *Acta Metall.*, 1988, **36**, p 871–882
2. M. Hagiwara, A. Araoka, S.J. Yang, S. Emura, and S.W. Nam, The Effect of Lamellar Morphology on Tensile and High-Cycle Fatigue Behavior of Orthorhombic Ti-22Al-27Nb Alloy, *Metall. Mater. Trans. A*, 2004, **35A**, p 2161–2170
3. M. Hagiwara, S. Emura, A. Araoka, B.O. Kong, and F. Tang, Enhanced Mechanical Properties of Orthorhombic Ti2AlNb-Based Intermetallic Alloy, *Met. Mater. Int.*, 2003, **9**, p 265–272
4. T.K. Nandi and D. Banerjee, Creep of the Orthorhombic Phase Based on the Intermetallic Ti2AlNb, *Intermetallics*, 2000, **8**, p 915–928
5. J.H. Peng, Y. Mao, S.Q. Li, and X.F. Sun, Microstructure Controlling by Heat Treatment and Complex Processing for Ti2AlNb Based Alloys, *Mater. Sci. Eng. A*, 2001, **299**, p 75–80

6. A. Pathak and A.K. Singh, A First Principles Study of Ti2AlNb Intermetallic, *Solid State Commun.*, 2015, **204**, p 9–15
7. W. Wang, W.D. Zeng, C. Xue, X.B. Liang, and J.W. Zhang, Designed Bimodal Size Lamellar O Microstructures in Ti2AlNb Based Alloy: Microstructural Evolution, Tensile and Creep Properties, *Mater. Sci. Eng. A*, 2014, **618**, p 288–294
8. A.P. Wu, G.S. Zou, J.L. Ren, H.J. Zhang, G.Q. Wang, X. Liu, and M.R. Xie, Microstructures and Mechanical Properties of Ti-24Al-17Nb (at.%) Laser Beam Welding Joints, *Intermetallics*, 2002, **10**, p 647–652
9. G.L. Chen, Z.Q. Sun, and X. Zhou, Oxidation and Mechanical Behavior of Intermetallic Alloys in the Ti-Nb-Al Ternary System, *Mater. Sci. Eng. A*, 1992, **153**, p 597–601
10. J.K. Lee, M.H. Oh, and D.M. Wee, Long-Term Oxidation Properties of Al-Ti-Cr Two-Phase Alloys as Coating Materials for TiAl Alloys, *Intermetallics*, 2002, **10**, p 347–352
11. Z.L. Lei, Z.J. Dong, Y.B. Chen, L. Huang, and R.C. Zhu, Microstructure and Mechanical Properties of Laser Welded Ti-22Al-27Nb/TC4 Dissimilar Alloys, *Mater. Sci. Eng. A*, 2013, **559**, p 909–916
12. G. Çam and M. Koçak, Progress in Joining of Advanced Materials, *Int. Mater. Rev.*, 1998, **43**, p 1–44
13. G. Çam and M. Koçak, Progress in Joining of Advanced Materials—Part 1: Solid State Joining, Fusion Joining, and Joining of Intermetallics, *Sci. Technol. Weld. Join.*, 1998, **3**, p 105–126
14. G. Çam, Friction Stir Welded Structural Materials: Beyond Al-Alloys, *Int. Mater. Rev.*, 2011, **56**, p 1–48
15. P.L. Threadgill, The Prospects for Joining Titanium Aluminides, *Mater. Sci. Eng. A*, 1995, **192–193**, p 640–646
16. L.Q. Li, Y.B. Chen, C.L. Zhang, Z.L. Lei, and G.Y. Xu, Crystallization Behavior of Ti3Al-Nb Alloy Laser Beam Welding Joints, *Nonferrous Met. Soc. China*, 2005, **15**, p 16–20
17. L.J. Tan, Z.K. Yao, W. Zhou, H.Z. Guo, and Y. Zhao, Microstructure and Properties of Electron Beam Welded Joint of Ti-22Al-25Nb/TC11, *Aerosp. Sci. Technol.*, 2010, **14**, p 302–306
18. H.T. Zhang, P. He, J.C. Feng, and H.Q. Wu, Interfacial Microstructure and Strength of the Dissimilar Joint Ti3Al/TC4 Welded by the Electron Beam Process, *Mater. Sci. Eng. A*, 2006, **425**, p 255–259
19. Y.Y. Liu, Z.K. Yao, H.Z. Guo, and H.H. Yang, Microstructure and Property of the Ti-24Al-15Nb-1.5Mo/TC11 Joint Welded by Electron Beam Welding, *Int. J. Min Met. Mater.*, 2009, **16**, p 568–575
20. Z.L. Lei, Z.J. Dong, Y.B. Chen, J. Zhang, and R.C. Zhu, Microstructure and Tensile Properties of Laser Beam Welded Ti-22Al-27Nb Alloys, *Mater. Des.*, 2013, **46**, p 151–156
21. C. Qin, Z.K. Yao, Y.Z. Li, Y.Q. Ning, and H.Z. Guo, Effect of Hot Working on Microstructure and Mechanical Properties of TC11/Ti2AlNb Dual-Alloy Joint Welded by Electron Beam Welding Process, *Trans. Nonferrous Met. Soc. China*, 2014, **24**, p 3500–3508
22. K.Z. Zhang, M. Liu, Z.L. Lei, and Y.B. Chen, Microstructure Evolution and Tensile Properties of Laser-TIG Hybrid Welds of Ti2AlNb-Based Titanium Aluminide, *J. Mater. Eng. Perform.*, 2014, **23**, p 3778–3785
23. Q.J. Sun and G.C. Wang, Microstructure and Superplasticity of TA15 Alloy, *Mater. Sci. Eng. A*, 2014, **606**, p 401–408
24. J.C. Feng, H.Q. Wu, J.S. He, and B.G. Zhang, Microstructure Evolution of Electron Beam Welded Ti3Al-Nb Joint, *Mater. Charact.*, 2005, **54**, p 99–105
25. H.Q. Wu, J.C. Feng, J.S. He, and B.G. Zhang, Microstructure Evolution of High Nb Containing Ti3Al, Based Alloy Electron Beam Welding Joints, *Chin. J. Nonferr. Met.*, 2004, **14**, p 1313–1317
26. S. Kou, *Welding Metallurgy*, Wiley, New York, 1987
27. F. Tang, S. Nakazawa, and M. Hagiwara, The Effect of Quaternary Additions on the Microstructures and Mechanical Properties of Orthorhombic Ti2AlNb-based Alloys, *Mater. Sci. Eng. A*, 2002, **329**, p 492–498
28. R. Strychor, J.C. Williams, and W.A. Soffa, Phase Transformations and Modulated Microstructures in Ti-Al-Nb Alloys, *Metall. Mater. Trans. A*, 1988, **19**, p 225–234
29. K. Muraleedharan, A.K. Gogia, T.K. Nandy, D. Banerjee, and S. Lele, Transformations in a Ti-24Al-15Nb Alloy: Part I, Phase Equilibria and Microstructure, *Metall. Mater. Trans. A*, 1992, **23A**, p 401–415
30. J.W. Zhang, S.Q. Li, D.X. Zou, W.Q. Ma, and Z.Y. Zhong, Processing and Microstructure Control of ($\alpha_2 + B2 + O$) Alloy Sheet in Ti-Al-Nb System, *Intermetallics*, 2000, **8**, p 699–702
31. G.M. Reddy, T. Mohandas, and K. Chandreshekar, Observations on Welding of $\alpha(2) + O + \beta$ Titanium Aluminide, *Sci. Technol. Weld. Join.*, 2001, **6**, p 300–304
32. C.J. Boehlert, B.S. Majumdar, V. Seetharaman, and D.B. Miracle, The Microstructural Evolution in Ti-Al-Nb O + BCC Orthorhombic Alloys, *Metall. Mater. Trans. A*, 1999, **30**, p 2305–2323
33. G.S. Martin, C.E. Albright, and T.A. Jones, Evaluation of CO₂ Laser Beam Welding on a Ti3Al-Nb Alloy, *Weld. J.*, 1995, **74**, p 77–82
34. J. dos Santos, G. Çam, F. Torster, A. Insfran, S. Riekehr, V. Ventzke, and M. Koçak, Properties of Power Beam Welded Steels, Al- and Ti-Alloys: Significance of Strength Mismatch, *Weld. World*, 2000, **44**, p 42–64
35. B.G. Zhang, M.X. Shi, G.Q. Chen, and J.C. Feng, Microstructure and Defect of Titanium Alloy Electron Beam Deep Penetration Welded Joint, *Trans. Nonferrous Met. Soc. China*, 2012, **22**, p 2633–2637
36. J. Kumpfert and W.A. Kaysser, Orthorhombic Titanium Aluminides: Phases, Phase Transformations and Microstructure Evolution, *Zeitschrift fuer Metallkunde/Materials Research and Advanced Techniques*, 2001, **92**, p 128–134
37. W. Lu, Y.W. Shi, Y.P. Lei, and X.Y. Li, Effect of Electron Beam Welding on the Microstructures and Mechanical Properties of Thick TC4-DT Alloy, *Mater. Des.*, 2012, **34**, p 509–515
38. J. Kumpfert, Intermetallic Alloys Based on Orthorhombic Titanium Aluminide, *Adv. Eng. Mater.*, 2001, **3**, p 851–864